Geophysical Research Letters

RESEARCH LETTER
10.1029/2018GL078030

Key Points:
- Small particles in loose deposits are progressively eroded through water seepage, producing structural rearrangements and grain coarsening
- Local collapses can trigger a chain of processes that lead to slope failure and fluidization if the small erodible particles are abundant
- Coarsened deposits become less likely to fail and fluidize, making grain coarsening an effective healing process in coseismic deposits

Supporting Information:
- Supporting Information S1
- Movie S1
- Movie S2
- Movie S3
- Movie S4
- Movie S5
- Movie S6
- Movie S7
- Movie S8
- Movie S9
- Movie S10
- Movie S11
- Data Set S1

Correspondence to:
G. Scaringi,
g.scaringi@qq.com

Citation:
Hu, W., Scaringi, G., Xu, Q., & Huang, R. (2018). Internal erosion controls failure and runout of loose granular deposits: Evidence from flume tests and implications for postseismic slope healing. *Geophysical Research Letters*, *45*, 5518–5527. https://doi.org/10.1029/2018GL078030

Received 22 MAR 2018
Accepted 26 MAY 2018
Accepted article online 5 JUN 2018
Published online 9 JUN 2018

Internal Erosion Controls Failure and Runout of Loose Granular Deposits: Evidence From Flume Tests and Implications for Postseismic Slope Healing

Wei Hu[1], Gianvito Scaringi[1], Qiang Xu[1], and Runqiu Huang[1]

[1]State Key Laboratory of Geohazard Prevention and Geoenvironment Protection, Chengdu University of Technology, Chengdu, China

Abstract Landslides in granular soils can be highly hazardous when exhibiting flow-like behavior. The extensive mass wasting associated with the 2008 M_w = 7.9 Wenchuan earthquake (China) left several cubic kilometers of loose granular material deposited along steep slopes and in low-order channels. Rainfall-triggered remobilization of these deposits evolved often into catastrophic flow-like landslides. Ten years after the earthquake, most of the deposits are still in place but landslide rates have decreased significantly. Internal erosion-induced grain coarsening is one possible process producing this decrease. Through experiments on loose artificial slopes we demonstrate the major role of the internally erodible small grains in triggering failure and fluidization and producing grain coarsening. Under the same hydraulic boundary, if the erodible fraction is removed or reduced, the loose deposits remain stable or fail without fluidizing. Our results provide an experimental evidence to the patterns of sediment export and debris flows observed in nature after a strong earthquake.

Plain Language Summary Landslides exhibit a variety of behaviors, from imperceptible creep strains to catastrophic failures. Flow-like landslides are among the most hazardous, as they can happen suddenly and cover long distances at high speed. Strong earthquakes, such as the 2008 M_w = 7.9 Wenchuan earthquake (China), can cause extensive landsliding, feeding hillslopes and drainage channels with abundant debris. Rainfalls can remobilize these deposits, and the movement can evolve into catastrophic and deadly debris flows. Ten years after the Wenchuan earthquake, most of debris is still in place within the orogen, but landslide rates have decreased significantly. Various processes can strengthen the deposits of debris, reducing their susceptibility to failure. Among them, we show the role of the small granular fraction—that can be eroded and transported within the large soil pores—in triggering instability, failure, and fluidization of the deposits. If these small particles are fewer or absent, the deposits remain stable and water drains easily thanks to the higher hydraulic conductivity. In the light of our experiments, we suggest that a progressive removal of the small particles in absence of failure, which was observed in nature indirectly, can be one realistic process leading to the stabilization of the deposits.

1. Introduction

The 2008 M_w = 7.9 Wenchuan earthquake in China triggered extensive mass wasting (R. Huang & Fan, 2013) that left several cubic kilometers of loose debris hanging on steep hillslopes. Subsequent rainfall-triggered failures of many of these deposits generated catastrophic debris flows (Xu et al., 2012; S. Zhang et al., 2016). Flow-like landslides can initiate from excess pore pressure buildup, which can cause fluidization of both plastic and nonplastic soils, particularly when in a loose state (Iverson, 1997; Iverson et al., 1997, 2000; Picarelli et al., 2008). Experiments on artificial slopes (Okura et al., 2002; Take et al., 2004, 2014) showed different phases of slope collapse in loose sands, involving compaction and localized generation of excess pore pressures. Numerical works identified a mobility bifurcation at slope scale depending on pore pressure evolution controlled by void ratio and hydraulic conductivity (Iverson & George, 2016). On the other hand, excess pore pressures and fluidization have been suggested to be only the result of shear failure (Eckersley, 1990), with its cause to be ascribed to a different process. Despite the rich literature on flow-like landslides, the roles played by soil grading and its changes are still unclear. Mixtures of sand with silt-sized particles produce different modes of motion related to the different ability to dissipate the pore pressure

excess (G. Wang & Sassa, 2001, 2003). Investigations on loose artificial slopes (Hu et al., 2017, 2018) showed pore pressure buildup upon failure—positively correlated with the proportion of small particles—but without macroscopic vanishing of effective stresses. Seismic vibrations were found to occur before macroscopic pore pressure spikes and displacements (Hu et al., 2018), which were related to structural changes caused by seepage-induced migration of small grains. Similarly, high-frequency acoustic emissions were shown to precede the instability propagation and global failure (Jiang et al., 2017).

Here we present results of experiments on instrumented artificial loose granular slopes containing different proportions of small internally erodible particles subjected to various hydraulic boundaries. We monitor pore pressures and displacements together with seismic signals and acoustic emissions, and we quantify the internal erosion directly by sampling the slope material prior to failure. Finally, we discuss the results in the light of the observed decay of postearthquake landslide rates in the 2008 Wenchuan earthquake-affected area.

2. Materials and Methods

We use a granular soil sampled from a coseismic deposit that provided source material for a large debris flow (Hu et al., 2014; Xu et al., 2012). It consists of limestone fragments with specific gravity $G_s = 2.62$ and grain size from gravel to sand and silt (International Organization for Standardization, 2002), which were remixed to obtain the desired gradings (Figure 1a). The mixtures do not contain a plastic fraction of clayey nature (usually referred to as "fines") but are rich of fine-sand and silt-sized grains with the same lithology as that of the larger grains. Through preliminary experiments in which the particles transported by the water seepage outflowing from the artificial slopes are collected and analyzed (Figures 1b and 1d), we identify a threshold size d = 0.5 mm to discriminate between the small and the coarse fractions. This size matches, qualitatively, with that of the eroded particles transported as river-suspended sediments, which constitute a significant proportion (10%–26%) of the Wenchuan earthquake coseismic debris (G. Li et al., 2016; W. Wang et al., 2017). However, different thresholds may result from different grain assemblies having different pore structures.

We employ an instrumented flume, 3-m long and 0.4-m wide, with a floor slope of 28° (Figure 1c). We chose this value arbitrarily to allow for a variety of behaviors to be reproduced. Field investigations show failures in deposits of debris along slopes mostly of 20°–45°, originated from coseismic failures with modal slope ~30° (Marc et al., 2016). The side walls of the flume consist of transparent plexiglass sheets. The floor is covered by sand grains glued to a rubber sheet to reproduce an impervious high-frictional contact. Pore pressure transducers (water-saturated before the tests) are installed at the floor and at middepth within the slope. The transducers are not enclosed by filter materials that could damp their dynamic response. Basal displacements are measured through a 2-cm styrene foam ball connected by a stiff wire to a displacement transducer placed upslope and counterweighted at the other end. A 100 V/g accelerometer (Wilcoxon-731A/P31) is installed under the floor to detect seismic vibrations. In some tests, high-frequency (100–400 kHz) acoustic emissions (AEs) are also measured, using a high-sensitivity wideband AE transducer (Physical Acoustics, Mistral Group, Inc.) with 40-dB amplification installed on one side wall. A laser sensor is installed above the slope to measure vertical displacements of the mass prior to failure in a point 10 cm from the back of the slope (i.e., on the vertical of the pore pressure transducer No. 1, see Figure 1c). Artificial rainfall (65 mm/hr) from sprinklers mounted above the slope is used to trigger landsliding. A 0.39-m^2 board is installed in some tests to collect rainwater and produce a concentrated inflow from the top of the slope, roughly doubling the catchment area. Data recording from the sensors are synchronized through an acquisition system (NI-compact-DQA) with 1-kHz sampling frequency for the seismic vibrations and 1 MHz for the AEs. A laser scanner (Leica/ScanStation-2) with 0.1-mm accuracy is used to measure the postfailure topography.

We use mixtures containing up to 25% of small particles, prepared at a gravimetric water content w = 5%, poured in the flume and gently compacted in successive layers. The mass of each layer is chosen as such to yield a given thickness corresponding to an average skeleton void ratio $e_s = 0.42$, that is, a skeleton porosity $n_s = e_s/(1 + e_s) \approx 0.3$ and a skeleton relative density $RD_s \approx 0.12$ (with $RD_s = (e_{max} - e_s)/(e_{max} - e_{min})$, $RD_s = 0$ characterizing the material in its loosest state, $e_s = e_{max}$, and $RD_s = 1$ characterizing the densest possible state $e_s = e_{min}$). The so-built loose slopes are 25-cm thick, 110-cm long at the floor and 65-cm long at the top. The hydraulic conductivity k of the mixtures, evaluated by constant-head tests under $e_s = 0.42$, decreases from ~1 mm/s to ~0.1 mm/s with the content of small particles increasing from 0% to 25% (Figure 1e).

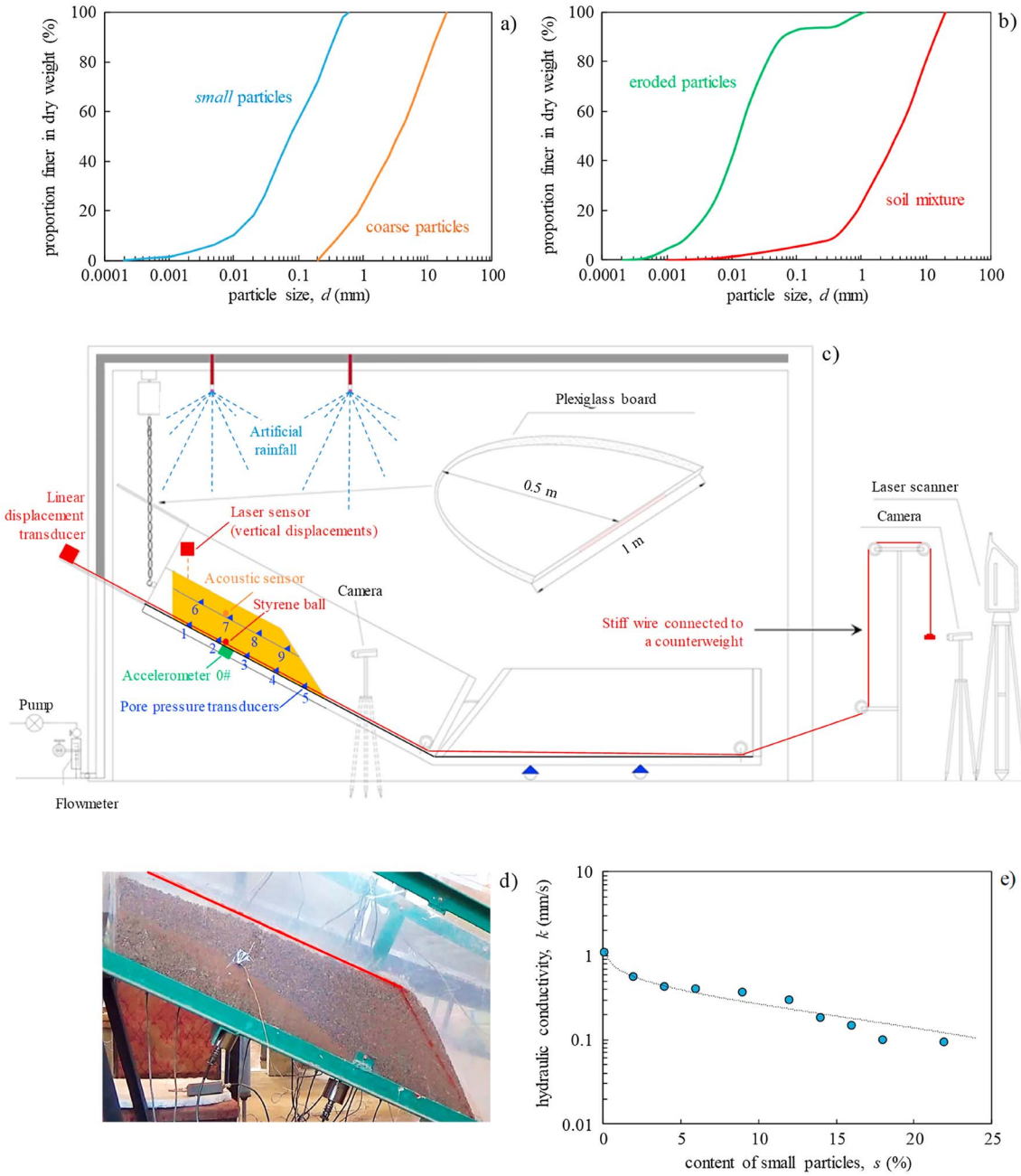

Figure 1. (a) Grading of the small the coarse fractions used in the experiments; (b) comparison between the initial soil grading and that of the eroded fraction, collected from the outflowing water at the slope toe; (c) se-up of the flume apparatus; (d) turbidity of the seepage water within the slope indicating transport of the small particles through the soil pores; and (e) hydraulic conductivity k of the soil mixtures prepared at $e_s = 0.42$ against the content of small particles (s, in percent dry weight). The trendline equation is $k = -0.185 \ln s + 0.6921$, with $R^2 = 0.98$.

3. Results

In Figures 2a and 2c we present the results of a test on a mixture containing 16% of small particles, with failure triggered by artificial rainfall and concentrated inflow. Basal positive pore pressures are detected at successive times moving downward along the flume floor, as the deposit becomes progressively saturated, while sensors at middepth respond to both rainfall infiltration and groundwater table rise. Negligible internal displacements occur before the macroscopic failure, while small vibration peaks occur throughout the test. The pore pressure spike does not precede the macroscopic failure. Pore pressures keep actually

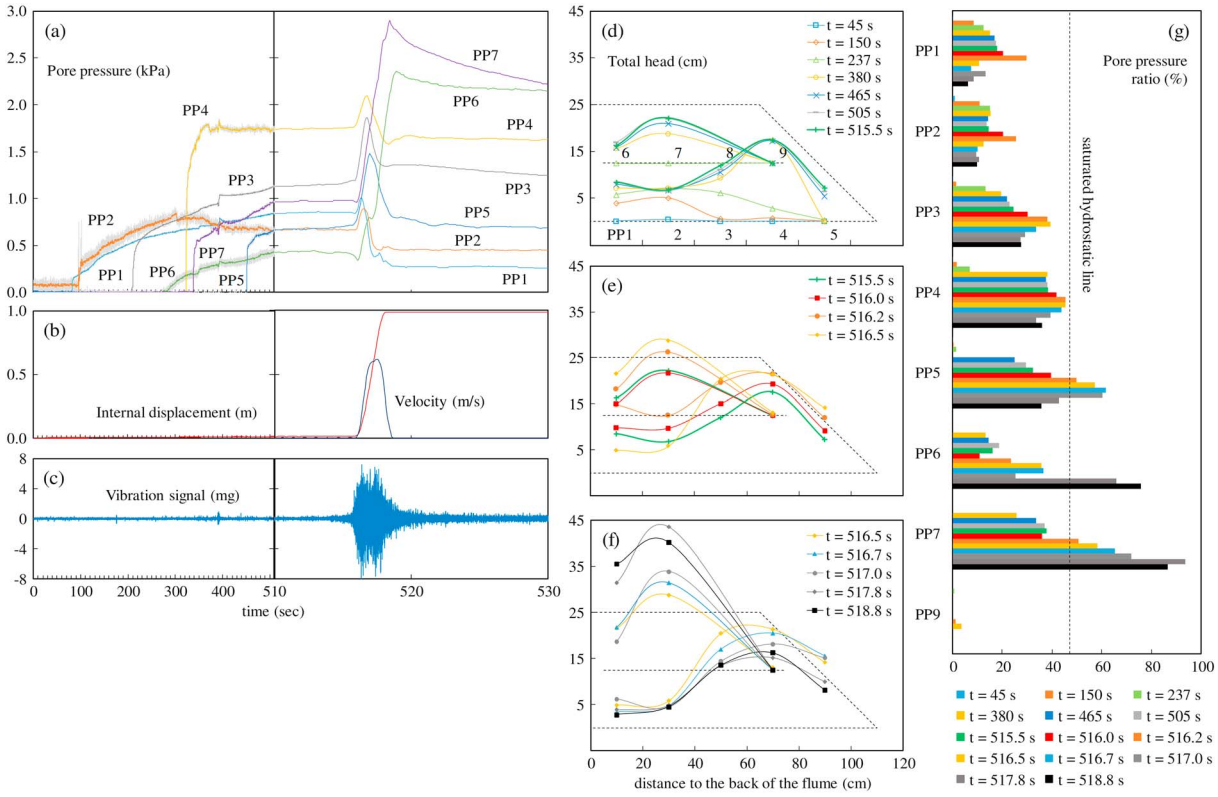

Figure 2. (a) Pore pressure, (b) internal displacement, and (c) vibration signal recorded during a flume test on the mixture with 16% small particles. Failure was triggered by artificial rainfall and concentrated water inflow. Total head (from the flume floor) evaluated at the flume floor and at midheight within the slope (d) before failure, (e) at failure, and (f) after failure. Pore pressure ratios at the same locations and times (g).

increasing at middepth during the movement, suggesting contractive behavior conducive to long runout (as demonstrated numerically by Iverson & George, 2016). Consistently with what observed by Hu et al. (2018), to whom the reader is referred to for additional details and examples, the intensity of the vibration recorded at the slope floor increases seconds before failure, and before any macroscopic deformation or pore pressure spike is recorded. Figures 2d and 2f show an estimation of the total hydraulic head at various locations at different times, under the simplifying assumption of hydrostatic pressure gradient. The response to the concentrated inflow occurs first (PP1–PP3), followed by a pressure increase near the toe (PP5) and at midslope (PP7) due to rainfall infiltration. The pore pressure distribution tends toward a steady state, maintained for comparatively long time (t = 380–515.5 s). At failure, pore pressures increase sharply at various locations, seemingly simultaneously, and pressure dissipation begins from the back of the slope, followed by the front and the shallow portions, which, therefore, may cover longer distances. This demonstrates that the mechanics of fluidized landslides, even at the reduced scale of our experiments with simplified 1-D-like geometry, cannot be expressed by traditional rheological formulas that evaluate local strength parameters only from local stress-strain states and rates (e.g., Iverson, 2003). On the contrary, as noted by Iverson and George (2016), realistic models must allow the apparent rheology to evolve in response to spatially distributed feedbacks.

We roughly quantified also the ratio of pore pressures u to the normal stress σ_n (Figure 2g), under the additional simplification of dry or saturated soil above or below the hypothesized groundwater table, respectively. The pore pressure ratio remains far from 100% both prior to and at failure, approaching this value only in the shallow soil during runout. In Figure S1 in the supporting information, slope topographies before and after failure and the height variations in each part are reported. The reader can examine the full test in Movies S1 and S2.

In Figure S2 we show an additional test on the same soil mixture in which failure was triggered only by artificial rainfall, which without the concentrated inflow, assuming a catchment size equal to the slope area. This

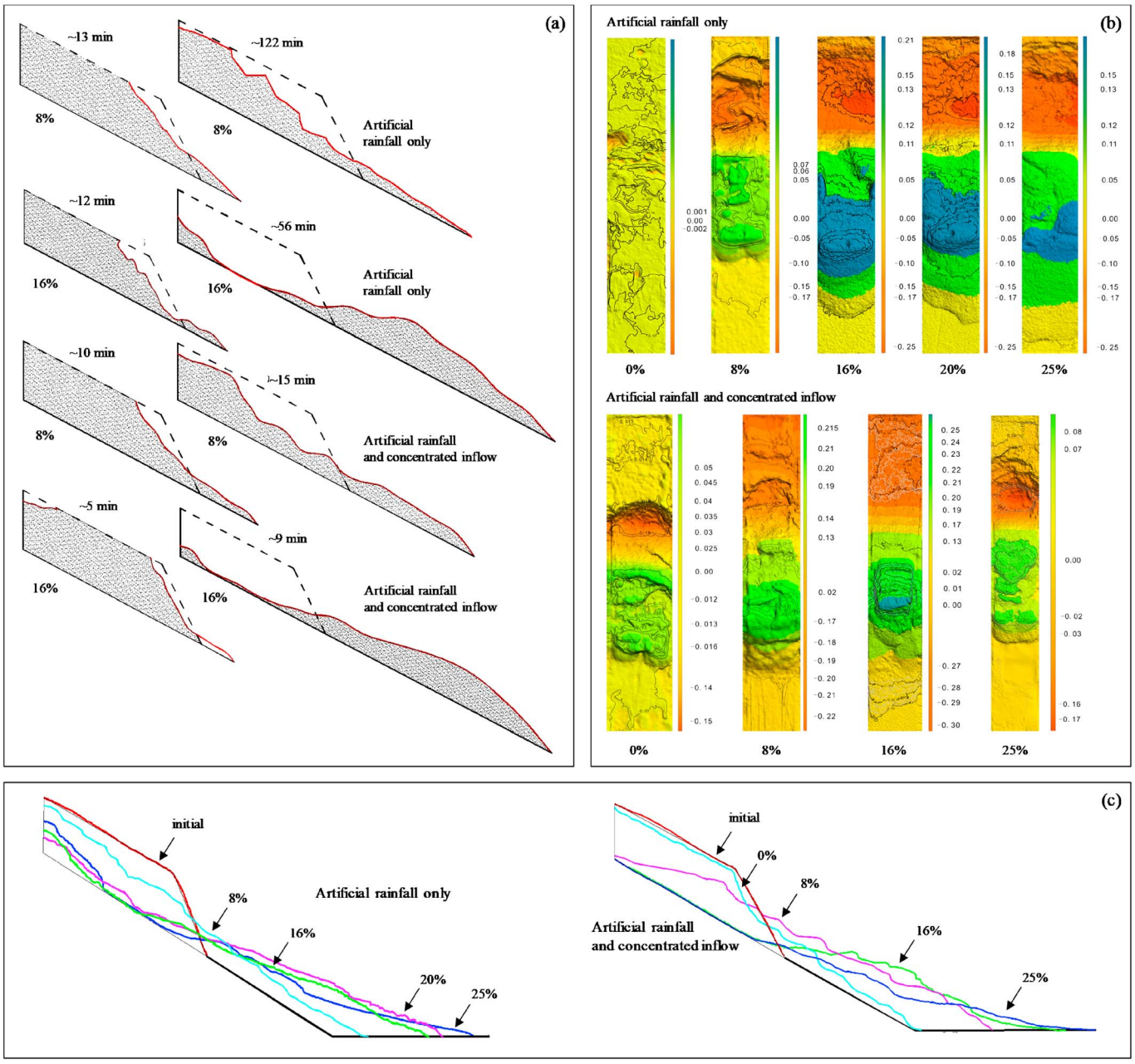

Figure 3. Flume tests on loose granular deposits with different proportions of small particles (0%–25%) under different hydraulic boundaries: (a) cartoons of longitudinal slope profiles at selected times during the tests; (b) height variations after the tests; and (c) final longitudinal profiles.

condition can be thought as more representative of the abundant coseismic deposits hanging high on the slopes (see, e.g., Gorum et al., 2011), close to the mountain ridges, while the condition of the test in Figure 2 is closer to that of the (also abundant) deposits in the lower portions of the slopes, which receive significant run-off water from upstream. Besides the much longer time to failure, pore pressures show more complexity, as wetting occurs primarily subvertically, by infiltration (Figures S2a and S2d). Local failures, displacements, and vibrations are recorded at various times during the tests (Figures S2b and S2c). Again, effective stresses seem far from vanishing (Figure S2e). However, sudden global failure does occur (Figure S2b), and the final slope topography (Figures S2f and S2g) is similar to that of the test shown in Figure 2, except for the back of the slope that did not fluidize because of the missing water inflow. Snapshots of the tests are shown in Figure S2g, while key test moments can be viewed in Movies S3–S5.

Tests on mixtures with different proportions of small particles (having different k and e, but constant e_s) are shown in Movies S6–S11. Postrunout topographies of the deposits are compared in Figures 3a–3c and S3. In particular, Figure 3a shows the slope profiles at key times during the tests, highlighting different processes occurring before the general failure: shallow sliding, retrogressive and rotational sliding, and diffuse settlements. Figure 3b shows the height variations after the tests, and Figure 3c shows the final slope profiles, highlighting the positive correlation between runout distance and the content of small particles. The different hydraulic boundaries produce topographic differences mostly in the rear of the slope. Quantitative comparisons of the tests are given in Figures 4a–4h. The settlement at the back of the slope (Figures 4a), which develops prior to the general failure, increases with the amount of small particles and is more pronounced under concentrated water inflow. The behavior is consistent with the higher likelihood of internal erosion and local collapses when small particles are abundant, under the same e_s. In fact, even though it is the sole e_s that determines the stress state corresponding to the onset of instability (Chu & Leong, 2002; Hu et al., 2017; S. L. Yang et al., 2006), a stress path leading to local instability and hence particle rearrangements and settlements can be produced more easily in mixtures rich in small particles having lower k that facilitates pore pressure buildup. Our tests also validate the counterintuitive conclusion reached by J. Yang et al. (2015) that even though high void ratios are conducive to instability, an increase of the global void ratio $e = n/(1 - n)$ (where n is the soil porosity) due to a decreasing proportion of small particles under a given e_s plays in favor of stability. Conversely, increasing e_s would increase the likelihood of instability (J. Yang et al., 2015) as the slope of the instability line would decrease and diverge from the critical state line, widening the space of unstable stress states at the expenses of the stable ones (Chu & Leong, 2002; Sasitharan et al., 1993; S. L. Yang et al., 2006). However, while some increase of e helps structural stability (through an increase of k), the large settlements observed under low e—that is, in mixtures rich in small particles—can only occur if these small particles can be eroded before the macroscopic collapse ultimately occurs and the slope undergoes runaway acceleration sustained by the high pore pressures.

In fact, in the slopes richer of small particles, failure occurs more rapidly and with longer runout, under generally higher pore pressures, with a more pronounced pressure spike and volume decrease (Figure 4). Conversely, in absence of small particles, macroscopic slope failure did not occur. Internal displacement, representative of the deep movement of the slope, is actually the largest for the mixture with 16% of small particles, while the final runout increases monotonically and is similar under the two hydraulic boundaries, being likely dominated by the movement of the shallow soil. Conversely, the pore pressure peak evaluated by PP3 near the flume floor is much smaller in the tests under artificial rainfall only than in those with rainfall plus water inflow. Finally, Figure 4h shows that the concentrated inflow reduces the time-to-failure greatly, while the tendency of the time to failure to decrease with the amount of small particles increasing is unaffected by the hydraulic boundary.

We compare the vibration signals at failure recorded during the tests with different proportions of small particles and different hydraulic boundaries in Figure S4 (supporting information). The signal length increases with the amount of small particles and so does the energy content (Figure S4h), highlighting the occurrence of a comparatively larger event. The analysis of the signal through the empirical mode decomposition (see N. Huang et al., 1998) with instantaneous frequencies determination (Hilbert-Huang transform) reveals that the mean frequency of the first intrinsic mode function (IMF1) of the signal tends to decrease with the amount of small particles, while its relative energy content slightly increases (Figures S4i and S4j). The IMFs highlight information at different scales, and they are characterized by decreasing frequencies and energy contents moving toward higher modes. While the lowest frequencies can be associated with the resonant modes of the flume structure, the highest ones (200–400 Hz in our experiments) must be related to the scale of particles interactions (Hu et al., 2018).

Additional tests with different proportions of small particles and different hydraulic boundaries are reported in Figures S5–S7 (supporting information, replotted from Hu et al., 2018). Further tests were performed using a flume apparatus with different slope inclination and geometry (Figure S8), to exclude the effect of the latter on the observed processes (replotted from Hu et al., 2017). A representative test result is given in Figure S9, and summaries of several tests are presented in Figures S10–S12. Similarities with our original results in terms of pore pressures evolution and ratios, displacements, and seismic signals are evident. This gives us confidence that the observed failure and runout processes are independent of the flume setup and relatively

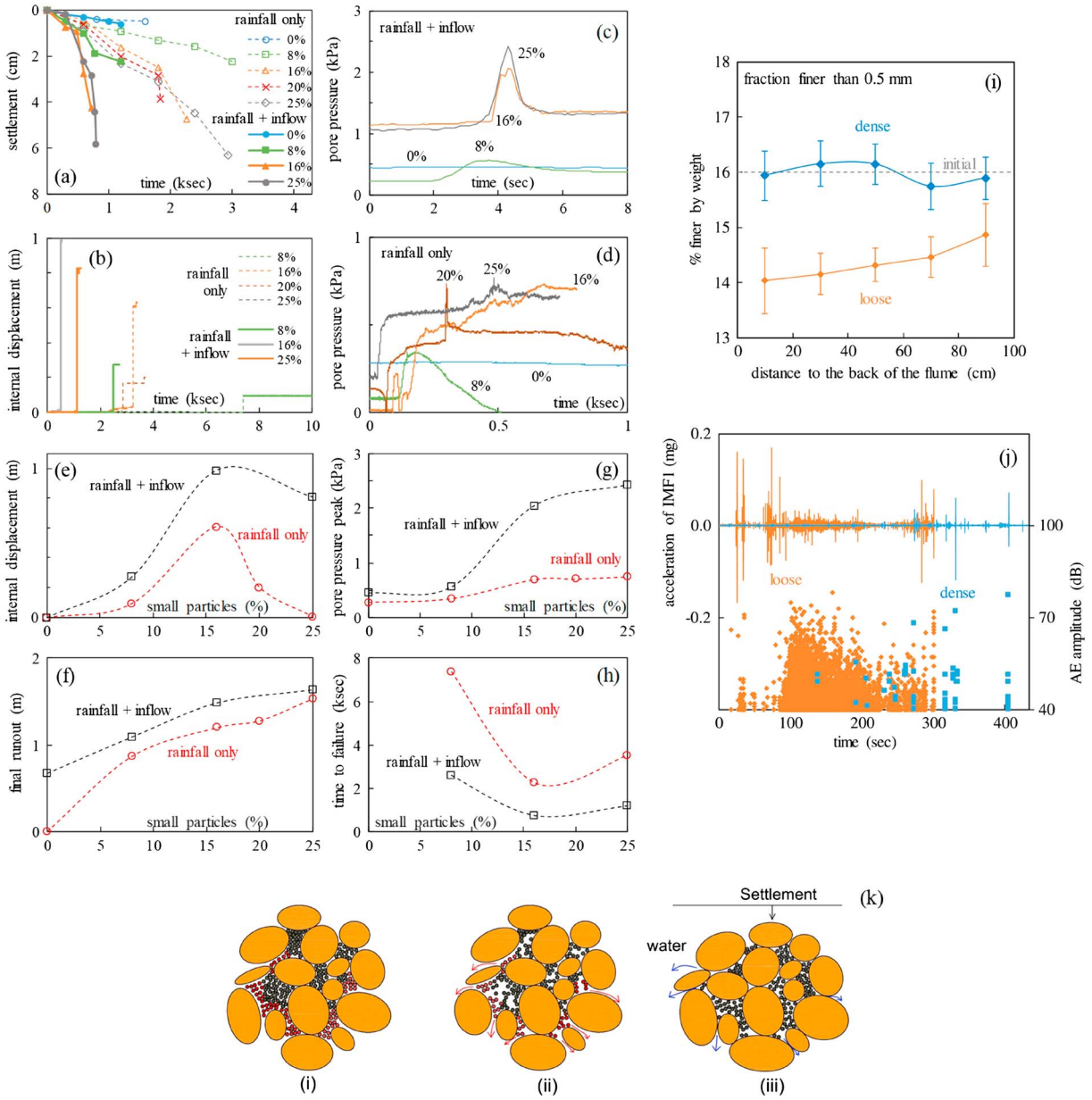

Figure 4. Settlement at the top of the slope (a) and internal displacement (b) against time since the beginning of the test. Pore pressure peak at PP3 against time for tests with artificial rainfall plus water inflow (c) and artificial rainfall only (d). Internal displacement (e), final runout distance (f), pore pressure peak at PP3 (g), and time to failure (h) against the content of small particles. Internal erosion by seepage water (i) revealed by the spatial variability of soil grading prior to failure (tests performed with 16% small particles by increasing the water level from the back of the flume): loose soil, 12% relative density and dense soil, and 81% relative density. Vibration signal (first intrinsic mode function, IMF1) and acoustic emissions (AE) during the same tests (j). Sketch of grain coarsening and consolidation mechanism by internal erosion (k).

insensitive to the type of hydraulic boundary that triggers the event and therefore must be controlled by the slope material and structure.

Hints of internal erosion and transport of small particles by water seepage were shown in Figure 1, together with the grading of the eroded soil fraction (Figures 1b and 1d). In Figure 4i we show the grading of small and coarse fractions, sampled near the bottom of the slope (at locations corresponding to PP1–5, see Figure 1c) after additional tests that were interrupted before the slope collapse. Due to seepage, small particles are found in concentrations that increase toward the toe of the slope in the loose granular assembly (from 1 to 5 in Figure 4i), and a portion of them is able to escape from the slope before failure. Internal erosion is

possible only if the structure is sufficiently loose, with the pores being sufficiently large to let the small particles migrate, and if the hydraulic gradient is strong enough to transport them (Figure 4k). In fact, as shown in Figure 4i, if the slope is prepared at high relative density (81%), there is no evidence of internal erosion, and the slope shows stable behavior after prolonged seepage. Evidences of particle rearrangements and internal erosion are also given by the vibrations (IMF1 of the Hilbert-Huang transform) and AEs recorded during the test on the loose granular slope (Figure 4j). Conversely, much fewer AEs and much smaller and less frequent vibrations were emitted by the denser material, in which internal erosion was absent or negligible. Vibrations can result from a variety of processes occurring during the tests. As discussed in Hu et al. (2018), low-frequency (and low-energy) emissions can be associated to ambient noise and vibrations of the assembly as a whole or of the experimental apparatus, of which they match the modal frequencies. Conversely, the highest-frequency (and highest-energy) emissions, such as those captured by the IMF1 and especially by the AEs, can be only associated to signal sources of millimetric and centimetric scales, such as collisions, rearrangements, and migration of the smallest grains.

4. Discussion

Coseismic landslide deposits are very sensitive to hydrological inputs soon after the earthquake (e.g., Hovius et al., 2011; R. Huang & Fan, 2013; Marc et al., 2015; Yu et al., 2014). However, this high sensitivity is short lived, as landslide-triggering rainfall thresholds and landslide rates tend to normalize quickly, in about a decade (Marc et al., 2015; W. Wang et al., 2017; W. Yang et al., 2017). Enhanced mass wasting and fluvial sediment evacuation following the Wenchuan earthquake can only account for the depletion of a small proportion of the coseismic debris (W. Wang et al., 2017; S. Zhang et al., 2016; S. Zhang & Zhang, 2017), while most of it stabilized along the slopes, within the orogen. Various mechanisms have been proposed to explain the postseismic healing in place of the coseismic debris, such as progressive revegetation, consolidation, and grain coarsening (e.g., L. Li et al., 2015; Lin et al., 2006; Saba et al., 2010). However, during just a few years, revegetation can only produce limited soil strength increase, variation of infiltration capability, and decrease of erodibility (and only in the shallow soil, as complete restoration of deep-rooted arboreal vegetation may require several decades). Therefore, revegetation seems insufficient to explain the fast decaying landslide rates that have been observed, particularly among large (and deep) deposits of debris, and the abundancy of stable but not yet revegetated deposits. Conversely, consolidation (i.e., compaction or densification) of the loose deposits induced by water seepage is a plausible process that limits the contractive behavior and makes fluidization less likely. However, under a given skeleton void ratio, e_s, compaction in absence of internal erosion seems less likely to be the dominating process in soils rich in small particles, which are the most susceptible to failure and fluidization. This seems reasonable because (1) soils rich in small particles have smaller global void ratios, e, and hence less room for compaction, unless more room is provided through internal erosion; and (2) they are subjected to smaller seepage forces, due to their much lower k, which may be insufficient to force rearrangements of the coarse grains. These processes, however, may well occur in coarse-only assemblies (although they may require much stronger, thus less probable, hydrological inputs, and hydraulic gradients) and may occur in any case if promoted by seismicity (see Brain et al., 2017).

In our tests we see the small, erodible soil fraction playing a fundamental control on the failure mechanism and runout of flow-like landslides in loose deposits. Under the same hydraulic boundary and e_s, coarse-only deposits are much less susceptible to failure, while deposits with significant small-sized fraction (8%–25%)—that can be produced, for instance, by large rock avalanching with intense distributed fragmentation (Dufresne & Dunning, 2017; M. Zhang & McSaveney, 2017)—can fail dramatically and exhibit fluidization and long runout. The proportion of small erodible particles correlates positively with the runout distance but negatively with the landslide-triggering rainfall threshold (the rainfall duration, in this case). It seems also reasonable that the deposits rich in small particles, being the most likely to fail, may be removed from the hillslopes quicker than the coarser deposits. Field evidence of changing initiation and runout mechanisms of debris flows related to grain coarsening of the source deposits was shown by S. Zhang et al. (2014). While studying the debris flow patterns in a catchment in the Wenchuan earthquake-affected area, the authors observed that initiation of debris flow by failure of hillslope loose deposits (such as those simulated in this work) became progressively less likely as the depletion of the finest fraction proceeded, while other mechanisms became dominant, which involved predominantly the failure of channelized material, which was subjected to a comparatively much larger water input from upstream.

Failure during the flume tests was shown to occur after a steady state positive pore pressure distribution had been reached at the bottom of the slope. The time required for the saturation and pore pressure buildup is controlled by k (see also Hu et al., 2017), which decreases significantly with the amount of small particles and therefore affects significantly, in turn, the time to failure and the landslide-triggering rainfall threshold. On the other hand, internal erosion by water seepage and migration of the small-sized fraction does occur well before the general failure, as suggested by the seismic and acoustic precursory signals and revealed by the changing soil grading (Figure 4i), resulting in microstructural rearrangements that produce progressive consolidation (densification) and grain coarsening. If failure is not reached—for instance, if the hydrological input is insufficient or short lasted and sufficient time is allowed for the pore pressures to dissipate (i.e., if the role of antecedent rainfall can be excluded)—the coarsened and densified slope will be less susceptible to failure during the subsequent hydrological event. This is consistent with the observed recovery of the landslide-triggering rainfall thresholds after the coseismic drop (e.g., Yu et al., 2014). Evidences of enhanced erosion of small particles and transport through the fluvial network following the 2008 Wenchuan earthquake were also shown, for instance, by G. Li et al. (2016) and G. Wang et al. (2017). Progressive grain coarsening and its influence on successive debris flow events was also pointed out by S. Zhang et al. (2014), who showed, in particular, that the first large debris flow may deplete a significant portion of the small-sized fraction. Moreover, enhanced sediment fluxes—related to the erosion of the small-grained coseismic landslide material that resides in the hillslope domain (G. Li et al., 2016)—were shown to decay toward background levels during a time span consistent with that of the enhanced landslide rates. This gives confidence that a causal relation between the decreasing landslide susceptibility and the progressive healing of the coseismic deposits caused by internal erosion-induced grain coarsening and consolidation is likely also at field scale and is worth of being verified through field-scale investigations.

5. Conclusion

We presented experiments on artificial loose granular deposits subjected to landsliding induced through various hydraulic boundaries, and we highlighted the role of the small-sized, erodible soil fraction on the landslide failure mechanism, runout distance, and landslide-triggering rainfall. Reduced hydraulic conductivity and local instability induced by internal erosion control the process. This is suggested by slope settlements during water seepage, by seismic and acoustic precursory signals, and by direct measurements of particles grading prior to failure. Frequent hydrologically triggered failures of co-seismic loose deposits, often evolving in flow-like landslides, were observed in the years following the Wenchuan earthquake. Landslide activity is now returning to pre-earthquake levels but most of deposits are still in place and are largely stabilized. Internal erosion of small particles—and their progressive removal through the large-pores network of the loose deposits—can explain the initially high but then decaying susceptibility to failure of the coseismic deposits. Erosion of small particles is consistent with the patterns of fluvial sediments evacuation: it produces progressive grain coarsening as observed in the field and leads to increasing landslide-triggering rainfall thresholds and decreasing susceptibility to failure.

Acknowledgments
This research was supported by the Key Program of the National Natural Science Foundation of China (grant 41630640), the Basic Research Funds (41790433), and the Funds for Creative Research Groups of China (41521002). The original data used in this work can be retrieved from the data set available in the supporting information. Non-original data can be obtained from the respective references. We acknowledge inputs and constructive comments from Mauri McSaveney and M. Bayani Cardenas and four anonymous reviewers.

References

Brain, M. J., Rosser, N. J., & Tunstall, N. (2017). The control of earthquake sequences on hillslope stability. *Geophysical Research Letters*, *44*(2), 865–872. https://doi.org/10.1002/2016GL071879

Chu, J., & Leong, W. K. (2002). Effect of fines on instability behaviour of loose sand. *Géotechnique*, *52*(10), 751–755. https://doi.org/10.1680/geot.2002.52.10.751

Dufresne, A., & Dunning, S. A. (2017). Process dependence of grain size distributions in rock avalanche deposits. *Landslides*, *14*(5), 1555–1563. https://doi.org/10.1007/s10346-017-0806-y

Eckersley, D. (1990). Instrumented laboratory flowslides. *Géotechnique*, *40*, 489–502. https://doi.org/10.1680/geot.1990.40.3.489

Gorum, T., Fan, X., van Westen, C. J., Huang, R., Xu, Q., Tang, C., & Wang, G. (2011). Distribution pattern of earthquake-induced landslides triggered by the 12 May 2008 Wenchuan earthquake. *Geomorphology*, *133*(3-4), 152–167. https://doi.org/10.1016/j.geomorph.2010.12.030

Hovius, N., Meunier, P., Ching-Weei, L., Hongey, C., Yue-Gau, C., Dadson, S., et al. (2011). Prolonged seismically induced erosion and the mass balance of a large earthquake. *Earth and Planetary Science Letters*, *304*(3-4), 347–355. https://doi.org/10.1016/j.epsl.2011.02.005

Hu, W., Hicher, P.-Y., Scaringi, G., Xu, Q., van Asch, T. W. J., & Wang, G. (2018). Seismic precursor to instability induced by internal erosion in loose granular slopes. *Géotechnique*. https://doi.org/10.1680/jgeot.17.p.079

Hu, W., Scaringi, G., Xu, Q., Pei, Z., van Asch, T. W. J., & Hicher, P.-Y. (2017). Sensitivity of the initiation and runout of flowslides in loose granular deposits to the content of small particles: An insight from flume tests. *Engineering Geology*, *231*, 34–44. https://doi.org/10.1016/j.enggeo.2017.10.001

Hu, W., Xu, Q., van Asch, T. W. J., Zhu, X., & Xu, Q. Q. (2014). Flume tests to study the initiation of huge debris flows after the Wenchuan earthquake in S-W China. *Engineering Geology*, *182*, 121–129. https://doi.org/10.1016/j.enggeo.2014.04.006

Huang, N. E., Shen, Z., Long, S. R., Wu, M. C., Shih, H. H., Zheng, Q., et al. (1998). The empirical mode decomposition and the Hilbert spectrum for nonlinear and nonstationary time series analysis. *Proceedings of the Royal Society of London*, *454*(1971), 903–995. https://doi.org/10.1098/rspa.1998.0193

Huang, R., & Fan, X. (2013). The landslide story. *Nature Geoscience*, *6*(5), 325–326. https://doi.org/10.1038/ngeo1806

International Organization for Standardization (2002). Geotechnical investigation and testing—Identification and classification of soil—Part 1: Identification and description, 12 pp., ref. ISO 14688–1:2002, International Organization for Standardization, Geneva, Switzerland.

Iverson, R. M. (1997). The physics of debris flows. *Reviews of Geophysics*, *35*(3), 245–296. https://doi.org/10.1029/97RG00426

Iverson, R. M. (2003). The debris-flow rheology myth. In C. L. Cheng & D. Rickenmann (Eds.), *Debris-flow hazards mitigation: Mechanics, prediction, and assessment* (Vol. 1, pp. 303–314). Rotterdam, the Netherlands: Millpress.

Iverson, R. M., & George, D. L. (2016). Modelling landslide liquefaction, mobility bifurcation and the dynamics of the 2014 Oso disaster. *Géotechnique*, *66*(3), 175–187. https://doi.org/10.1680/jgeot.15.LM.004

Iverson, R. M., Reid, M. E., Iverson, R. N., LaHusen, R. G., Logan, M., Mann, J. E., & Brien, D. L. (2000). Acute sensitivity of landslide rates to initial soil porosity. *Science*, *290*(5491), 513–516. https://doi.org/10.1126/science.290.5491.513

Iverson, R. M., Reid, M. E., & LaHusen, R. G. (1997). Debris flow mobilization from landslides. *Annual Review of Earth and Planetary Sciences*, *25*(1), 85–138. https://doi.org/10.1146/annurev.earth.25.1.85

Jiang, Y., Wang, G., & Kamai, T. (2017). Acoustic emission signature of mechanical failure: Insights from ring-shear friction experiments on granular materials. *Geophysical Research Letters*, *44*, 2782–2791. https://doi.org/10.1002/2016GL071196

Li, G., West, A. J., Densmore, A. L., Hammond, D. E., Jin, Z., Zhang, F., et al. (2016). Connectivity of earthquake-triggered landslides with the fluvial network: Implications for landslide sediment transport after the 2008 Wenchuan earthquake. *Journal of Geophysical Research: Earth Surface*, *121*, 703–724. https://doi.org/10.1002/2015JF003718

Li, L., Yao, X., Zhang, Y., Iqbal, J., Chen, J., & Zhou, N. (2015). Surface recovery of landslides triggered by 2008 Ms8.0 Wenchuan earthquake (China): A case study in a typical mountainous watershed. *Landslides*, *13*(4), 787–794. https://doi.org/10.1007/s10346-015-0594-1

Lin, W.-Z., Lin, C.-Y., & Chou, W.-C. (2006). Assessment of vegetation recovery and soil erosion at landslides caused by a catastrophic earthquake: A case study in Central Taiwan. *Ecological Engineering*, *28*(1), 79–89. https://doi.org/10.1016/j.ecoleng.2006.04.005

Marc, O., Hovius, N., Meunier, P., Gorum, T., & Uchida, T. (2016). A seismologically consistent expression for the total area and volume of earthquake-triggered landsliding. *Journal of Geophysical Research: Earth Surface*, *121*, 640–663. https://doi.org/10.1002/2015JF003732

Marc, O., Hovius, N., Meunier, P., Uchida, T., & Hayashi, S. (2015). Transient changes of landslide rates after earthquakes. *Geology*, *43*(10), 883–886. https://doi.org/10.1130/G36961.1

Okura, Y., Kitahara, H., Ochiai, H., Sammori, T., & Kawanani, A. (2002). Landslide fluidization process by flume experiments. *Engineering Geology*, *66*(1-2), 65–78. https://doi.org/10.1016/S0013-7952(02)00032-7

Picarelli, L., Olivares, L., Comegna, L., & Damiano, E. (2008). Mechanical aspects of flow-like movements in granular and fine grained soils. *Rock Mechanics and Rock Engineering*, *41*(1), 179–197. https://doi.org/10.1007/s00603-007-0135-x

Saba, S. B., van der Meijde, M., & van der Werff, H. (2010). Spatiotemporal landslide detection for the 2005 Kashmir earthquake region. *Geomorphology*, *124*(1-2), 17–25. https://doi.org/10.1016/j.geomorph.2010.07.026

Sasitharan, S., Robertson, P. K., Sego, D. C., & Morgenstern, N. R. (1993). Collapse behavior of sand. *Canadian Geotechnical Journal*, *30*(4), 569–577. https://doi.org/10.1139/t93-049

Take, W. A., Beddoe, R. A., Bilesavar, R. D., & Phillips, R. (2014). Effect of antecedent groundwater conditions on the triggering of static liquefaction landslides. *Landslides*, *12*(3), 469–479. https://doi.org/10.1007/s10346-014-0496-7

Take, W. A., Bolton, M. D., Wong, P. C. P., & Yeung, F. J. (2004). Evaluation of landslide triggering mechanisms in model fill slopes. *Landslides*, *1*(3), 173–184. https://doi.org/10.1007/s10346-004-0025-1

Wang, G., & Sassa, K. (2001). Factors affecting rainfall-induced flowslides in laboratory flume tests. *Géotechnique*, *51*(7), 587–599. https://doi.org/10.1680/geot.2001.51.7.587

Wang, G., & Sassa, K. (2003). Pore-pressure generation and movement of rainfall-induced landslides: Effects of grain size and fine-particle content. *Engineering Geology*, *69*(1–2), 109–125. https://doi.org/10.1016/S0013-7952(02)00268-5

Wang, W., Godard, V., Liu-Zheng, J., Scherler, D., Xu, C., Zhang, J., et al. (2017). Perturbation of fluvial sediment fluxes following the 2008 Wenchuan earthquake. *Earth Surface Processes and Landforms*, *42*(15), 2611–2622. https://doi.org/10.1002/esp.4210

Xu, Q., Zhang, S., Li, W. L., & van Asch, T. W. J. (2012). The 13 August 2010 catastrophic debris flows after the 2008 Wenchuan earthquakes, China. *Natural Hazards and Earth System Sciences*, *12*(1), 201–216. https://doi.org/10.5194/nhess-12-201-2012

Yang, J., Wei, L. M., & Dai, B. B. (2015). State variables for silty sands: Global void ratio or skeleton void ratio? *Soils and Foundations*, *55*(1), 99–111. https://doi.org/10.1016/j.sandf.2014.12.008

Yang, S. L., Sandven, R., & Grande, L. (2006). Instability of sand-silt mixtures. *Soil Dynamics and Earthquake Engineering*, *26*(2-4), 183–190. https://doi.org/10.1016/j.soildyn.2004.11.027

Yang, W., Qi, W., Wang, M., Zhang, J., & Zhang, Y. (2017). Spatial and temporal analyses of post-seismic landslide changes near the epicentre of the Wenchuan earthquake. *Geomorphology*, *276*, 8–15. https://doi.org/10.1016/j.geomorph.2016.10.010

Yu, B., Wu, Y., & Chu, S. (2014). Preliminary study of the effect of earthquakes on the rainfall threshold of debris flows. *Engineering Geology*, *182*, 130–135. https://doi.org/10.1016/j.enggeo.2014.04.007

Zhang, M., & McSaveney, M. J. (2017). Rock-avalanche deposits store quantitative evidence on internal shear during runout. *Geophysical Research Letters*, *44*, 8814–8821. https://doi.org/10.1002/2017GL073774

Zhang, S., & Zhang, L. (2017). Impact of the 2008 Wenchuan earthquake in China on subsequent long-term debris flow activities in the epicentral area. *Geomorphology*, *276*, 86–103. https://doi.org/10.1016/j.geomorph.2016.10.009

Zhang, S., Zhang, L., Lacasse, S., & Nadim, F. (2016). Evolution of mass movements near epicentre of Wenchuan earthquake, the first eight years. *Scientific Reports*, *6*(1), 36154. https://doi.org/10.1038/srep36154

Zhang, S., Zhang, L. M., & Chen, H. X. (2014). Relationships among three repeated large-scale debris flows at Pubugou Ravine in the Wenchuan earthquake zone. *Canadian Geotechnical Journal*, *51*(9), 951–965. https://doi.org/10.1139/cgj-2013-0368